Geoderma 461 (2025) 117460

Contents lists available at ScienceDirect

Geoderma

journal homepage: www.elsevier.com/locate/geoderma

High-resolution electrical resistivity tomography for quantitative interpretation of sub-surface karst structures: A case study in Southwest China

Weiwei Jiang [a,b,c], Tao Peng [a,b,c,*], Xingbao Zhang [c,d], Shijie Wang [a,b,c], Zargham Mohammadi [e], Zhanyu Tang [a,c]

[a] State Key Laboratory of Environment Geochemistry, Institute of Geochemistry, Chinese Academy of Sciences, Guiyang 550081, China
[b] University of Chinese Academy of Sciences, Beijing 100049, China
[c] Puding Karst Ecosystem Research Station, Chinese Academy of Sciences, Puding 562100, China
[d] Key Laboratory of Mountain Environment Evolution and Regulation, Institute of Mountain Hazards and Environment & Ministry of Water Resources, Chinese Academy of Sciences, Chengdu 610041, China
[e] Department of Earth Sciences, Faculty of Sciences, 7146713565, Shiraz University, Shiraz, Iran

ARTICLE INFO

Keywords:
Soil
Epikarst
Critical zone
Resistivity
Topographic characteristics
Southwest China

ABSTRACT

Soil-epikarst thickness and near surface characteristics are important components in understanding surface and groundwater interactions in karst environments. However, the complex lithological conditions, non-transparent rock and soil structures, and strong spatial heterogeneity limit the accurate quantification of soil thickness (ST) and epikarst thickness (EkT). In this study, we investigated the soil-epikarst structures and their spatial distribution at key topographic locations including different hillslope position, ridge, saddle, and valley using Electrical Resistance Tomography (5268 sampling points) in a peak cluster-valley catchment in Southwest China. The application of revised inflexion points in 1D resistivity vertical profiles for improving ST and EkT characterization accuracy was assessed, with interpretations validated against borehole data. The results show that compared with the interpretation accuracy of using a specific resistivity threshold at interfaces, the revised inflexion point of the 1D resistivity vertical profile significantly improved the interpretation accuracy of ST and EkT. The average ST in the valley (3.23 m) is much greater than that in hillslopes (0.49 m), while the average EkT in the valley (3.77 m) is smaller than that in hillslopes (3.93 m). The ST and EkT demonstrated a synchronous zonality variation pattern at different hillslope positions and valley. Plan and profile curvature, flow length up/down, aspect, and elevation are key topographic characteristics affecting EkT's spatial heterogeneity. The key findings of this study contribute to advancing the accurate interpretation of soil-epikarst structures under complex lithological conditions in karst areas, and support underground structural parameters for hydrological simulation at catchment scale.

1. Introduction

Soil thickness (ST) and epikarst thickness (EkT) are usually essential parameters for quantifying water and nutrient storage space of karst hydrological models, characterizing soil erosion and land productivity levels (Liu et al., 2013; Xu et al., 2020). ST is the depth from the surface to consolidated material (Kuriakose et al., 2009; Zhang et al., 2022). The epikarst zone is located in the upper part of the vadose zone with multiple water-conducting media such as fissures, fractures, and conduits and has a lower boundary of undeveloped compact bedrock (Al-Fares et al., 2002; Hartmann et al., 2014; Williams, 2008). Due to the high spatial heterogeneity that occurs during the epikarst development and limitations of underground exploration techniques, accurate interpretation of the soil-epikarst in complex lithology sites is challenging (Kuriakose et al., 2009; Carrière et al., 2013; Alfuqara and Anderson, 2023). Thus, understanding the structural information, distribution characteristics, feedback relationships, and key influencing factors for soil and epikarst zones in karst areas is of great significance for understanding epikarst evolution, supporting hydrological and solute transport process analysis, and reducing model uncertainty (Hartmann et al.,

* Corresponding author at: State Key Laboratory of Environment Geochemistry, Institute of Geochemistry, Chinese Academy of Sciences, Guiyang 550081, China.
E-mail address: pengtao@mail.gyig.ac.cn (T. Peng).

https://doi.org/10.1016/j.geoderma.2025.117460
Received 19 December 2024; Received in revised form 7 July 2025; Accepted 24 July 2025

2014; Xu et al., 2020).

Electrical resistivity tomography (ERT) is a widely used geophysical method with in-situ investigation for karst rock and soil structures and epikarst development degree (Binley et al., 2015; Chalikakis et al., 2011; Leopold et al., 2021; Yamakawa et al., 2012).The method, which calculates the spatio-temporal variability in resistivity (ρ, Ω·m) through the electrical potential field generated by injecting electrical current into the ground, can be used to characterize subsurface material structures as well as spatio-temporal changes in water content, fluid composition, and preferential flow (Alamry et al., 2017; Leopold et al., 2021). Given substantial differences in resistivity ranges between these materials (e.g., dry clay typically exhibits resistivity below 100 Ω·m, while limestone ranges from 60 to 10,000 Ω·m), some studies directly delineate the soil-epikarst interface and the epikarst-compact bedrock interface by setting different specific resistivity isopleth thresholds when estimating the ST and EkT (Chen et al., 2018; Cheng et al., 2019b; Tao et al., 2021). However, the current consideration highly relies on interpreters' experience and is somewhat subjective (Cheng et al., 2019a). Such method requires similar site conditions, and the results can only be used for rough comparisons of permeability conditions and epikarst development between different sampling areas (Chen et al., 2018). It is difficult to directly apply the estimated methods based on specific ρ thresholds to other sites because of different conditions in lithology, rock purity, moisture conditions, and data resolution between sites. On the other hand, Coulouma et al. (2013) proposed that when the average resistivity of the soil layer increases or decreases by 50 % relative to the average bedrock resistivity, the first clear inflexion point appears in the upper part of the vertical resistivity profile. High ρ contrast between soil and bedrock and the depth of the inflexion point can be used to estimate the soil–bedrock interface and ST (Alamry et al., 2017; Luo et al., 2024; Yamakawa et al., 2012). The permeability, weathering degree, and development of fissures in the epikarst zone decrease vertically with increasing depth (Wang et al., 2020; Wang et al., 2024). It can be inferred that ρ of the epikarst zone will exist significant variation until it reaches compact bedrock and stabilizes (Al-Fares et al., 2002; Williams 2008). Therefore, the position of the epikarst-compact bedrock interface is likely marked by another inflexion point, which forms the basis for estimating EkT. However, ρ is sensitive to factors such as lithology, purity, porosity, moisture content, and temperature (Alamry et al., 2017; Coulouma et al., 2013; Oyeyemi et al., 2022). Complex lithological conditions, non-transparent rock and soil structure, and rapid fluctuation in near surface moisture in karst areas result in vertical resistivity profiles that may lack the clear inflexion points or exhibit multiple ambiguous inflexion points. These uncertain points pose challenges for accurate interpreting the soil-epikarst-compact bedrock interface and estimating ST and EkT. Although interpretation uncertainties can be reduced through repeated resistivity surveys under different moisture conditions or by combining with other geophysical techniques, such approaches are more time-consuming and require careful assessment of the applicability of different geophysical techniques (Alamry et al., 2017; Carrière et al., 2013; Tao et al., 2021). Studies on interpreting these uncertain inflexion points and assessing the uncertainties they introduce remains relatively scarce. Accurately interpreting the soil-epikarst-compact bedrock interface and improving ST/EkT estimation form essential prerequisite for mapping ST/EkT distribution and reducing subsequent model input uncertainty.

Due to various factors such as climate, organisms, parent material, relief and time, there is a high degree of spatial heterogeneity in soil and epikarst development in karst areas (Jenny, 1941; Luo et al., 2024; Zhong et al., 2022). The observed EkT in karst areas worldwide ranges from one to tens of meters, with a typical average thickness of around 10 m (Al-Fares et al., 2002; Wilcox et al., 2008; Pardo-Igúzquiza et al., 2018). For a long time, researchers have been devoted to revealing the rock and soil structure, the relationship between ST and EkT, and their spatial distributions under strong heterogeneity features (Alfuqara and Anderson, 2023; Carrière et al., 2013; Yamakawa et al., 2012). For instance, a significant positive correlation between ST and EkT was identified, which emphasizes the co-evolution and positive feedback effect between soil and epikarst (Celico et al., 2010; Wang et al., 2024). The ST and EkT usually increase with the elevation decrease along the hillslope (Jenny, 1941; Zhang et al., 2013; Zhang et al., 2022). Cultivated land in the depression has larger ST and EkT, while the forest and grassland are smaller among different land cover type (Huang et al., 2021; Wang et al., 2022). Previous studies observe heterogeneity of soil and epikarst on hillslopes, runoff fields, and experimental plots (Chen et al., 2018; Gao et al., 2020; Luo et al., 2024). However, the studies have relatively small sampling lines/points and low sampling resolution, which is difficult to accurately model soil thickness and epikarst at catchment scales within complex karst topography (Alamry et al., 2017; Coulouma et al., 2013; Tao et al., 2021). Selecting the most effective environmental variables for predicting EkT are essential to mitigating model overfitting and enhancing model performance (Liu et al., 2013; Zhang et al., 2022). The spatial distribution characteristics and key controlling factors of rock and soil structures at important terrain and landform locations, including hillslope, ridge, saddle, concave-convex position, and valley, are still unclear, limiting the understanding of underground structural information at the catchment.

The karst region in southwestern China is one of the largest areas in the world where carbonate rocks are concentrated and continuously distributed, with an area of 540000 km^2. One hundred million residents in the area rely on karst groundwater resources (Xu et al., 2018). The peak cluster-depression (valley) is composed of conical hills and star-shaped valleys and is a typical karst landscape in the southwest karst region, accounting for about 73 % of the karst area (Wang et al., 2024). A peak cluster-valley catchment with complex lithological conditions in Guizhou Province, Southwest China, was selected to allow the study of ST and EkT's uncertainty in interpretation for improving ST and EkT estimation. The objectives of this study are to (1) assess application of 1D resistivity vertical profile revised inflection points for improved accuracy in ST and EkT characteristics; (2) investigate the spatial distribution and relationship of ST and EkT in a catchment scale, with focus on landforms and topographic locations including different hillslopes, slope position, saddle, concave-convex areas, and valley; (3) Identify the significance of select derivative topographic parameters for modeling EkT. We expect that the key finding of this study is that it can reduce uncertainty for the interpretation of non-transparent soil-epikarst structures under complex conditions between inter-sites and provide important underground structure information and parameter support for modelers.

2. Study area and methodology

2.1. Catchment description

The Chenqi catchment is in Puding County, Guizhou Province, southwestern China. It belongs to a typical cockpit karst landform with surrounding conical hillslopes (HS1-HS5 in Fig. 1) separated by a star-shaped valley. The drainage area is 1.26 km^2, with an elevation ranging from 1280 to 1470 m. The strata have inclination angle $< 9°$. The lithology is comprised on two limestone units underlain by dolomite inter-bedded with marl (profile of A-A', B-B'and C-C'in Fig. 1). The main land cover types include forest, shrubs, grassland, and cultivated land. The cultivated land is mainly distributed in valleys, downslopes and saddles, while other land cover types are randomly distributed. The study area belongs to the subtropical monsoon climate, with an average annual temperature of 15.2 ℃ and an average annual rainfall of 1315 mm, with 85 % concentrated from May to September. Such climatic characteristics results in highly developed epikarst zones pattern with conduits and fissures system and complex surface-underground hydrological processes in the catchment (Cheng et al., 2019a; Zhang et al., 2013). There are several karst springs in the hillslopes. In the valley, water flow moves through a seasonal surface river, and several

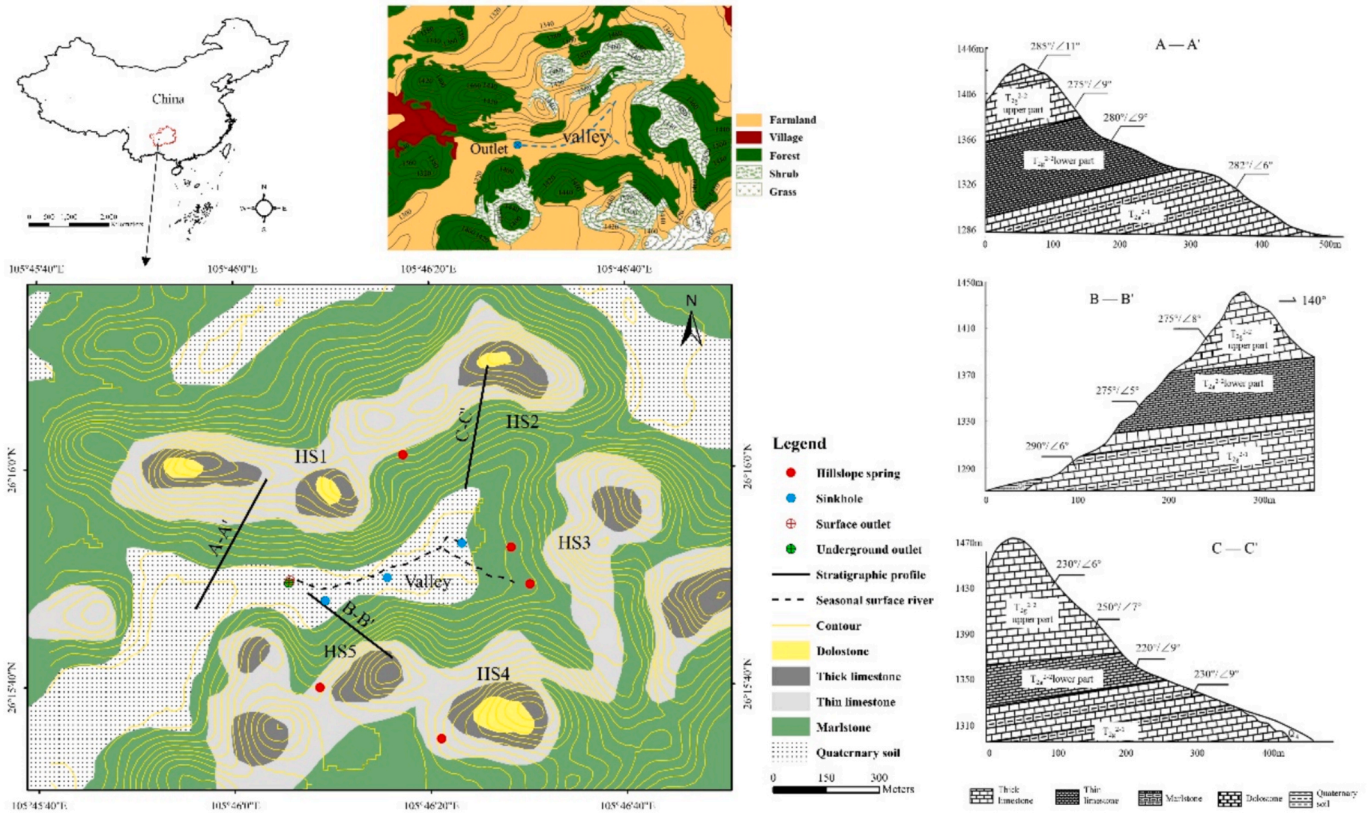

Fig. 1. Map of location, land use, topography, lithology, and three stratigraphic profiles of the Chenqi catchment.

natural sinkholes connected to the underground river then discharge into the surface/underground outlets (Fig. 1).

The Chenqi catchment is highly developed in the epikarst zone, with a carbonate rock outcrop rate of about 30 %, leading to strong underground leakage and a surface runoff coefficient of less than 5 % (Peng and Wang, 2012). The EkT on the hillslope was identified to be in a range of 2 ~ 13 m, with an average rock fissures rate of 5.3 % and hydraulic conductivity ranging from 10^{-3}-10^{-6} m/s (Zhang et al., 2013). In the valley, the ST is over 2 m, and the electrical resistivity of underground material has strong heterogeneity within 20 m in both horizontal and vertical directions (Chen et al., 2018; Cheng et al., 2019a).

2.2. Field geophysical survey

The position of the sampling lines is based on geological surveys and hillslope contour lines. The soil −epikarst structures of different hillslopes (HS1-HS5) were surveyed using ERT at various elevations, slope positions, curvatures, areas surrounding springs and lithological types from both horizontal and vertical directions from August to November 2023 (Fig. 2). The hillslope vertical lines (HS-VLs) continuously explore from saddle to downslope. The terrain of the sampling locations where the horizontal lines (HS-HLs) is located is relatively flat and straight. The elevation change within the same HS-HL is less than 1 m. The valley sampling lines (V-ILs) adopt an interlaced layout (Fig. 2). The HS-VLs and V-ILs are slightly curved because of the influence of steep terrain and dense crops (Fig. 2).

The Wenner array in ERT employs four collinear electrodes with equal spacing. The outer electrodes inject current into the ground, while the inner electrodes measure the resulting potential difference to calculate resistivity (Alao et al., 2024). This configuration is sensitive to vertical changes in the subsurface resistivity and has signal stability and noise immunity, making it suitable for near-surface investigations such as stratigraphic delineation and soil mapping (Leopold et al., 2021; Luo et al., 2024; Oyeyemi et al., 2022). In this study, the Wenner array was used for all ERT sampling lines. The detection depth can be calculated from the number of electrodes and inter-electrode spacing (Carrière et al., 2013). Each survey line uses 72 electrodes (Fig. 3). The inter-electrode spacing for hillslopes and valleys is set to 1 m and 2 m, corresponding to 12 m and 24 m detection depths, respectively. This setting can obtain a relatively high sampling resolution and satisfy the required detection depth in different landform types. Overall, the total sampling line number, sampling point number, and survey length within the whole catchment are 41, 5268, and 6.6 km, respectively (Table 1).

2.3. Interpreting soil-epikarst-compact bedrock interface

The acquisition system used for ERT survey is Syscal Pro (IRIS, Instruments, France). The acquired ERT data were processed using Prosys II and Res2dinv software, which produced 2D profiles of sampling lines and 1D resistivity ρ data of all sampling points through a least squares smoothness-constrained approach. The model of resistivity was considered as a simple three layer model with the soil, epikarst, and compact bedrock (Fig. 3). The first clear inflexion point was determined in the case of a significant increase (or decrease) of 50 % in the resistivity between various points in the upper part of the 1D vertical resistivity profile (Coulouma et al., 2013). However, no criteria exist for defining the epikarst-compact bedrock interface based on resistivity variations in previous studies. In this study, the second clear inflexion point was defined as no significant change in the resistivity (within 5 %) between various points in the lower part of the 1D vertical resistivity profile. The depth of the first and second inflexion points was considered as the inferred soil-epikarst interface and epikarst-compact bedrock interface, respectively. High-resolution ρ data (decimeter level in the vertical direction) were obtained after inversion because of short electrode spacing sampling in this study (Figs. 3-4). Thus, three horizontal lines with significant ρ differences (HS3-HL3 with thick limestone, HS3-HL4 with

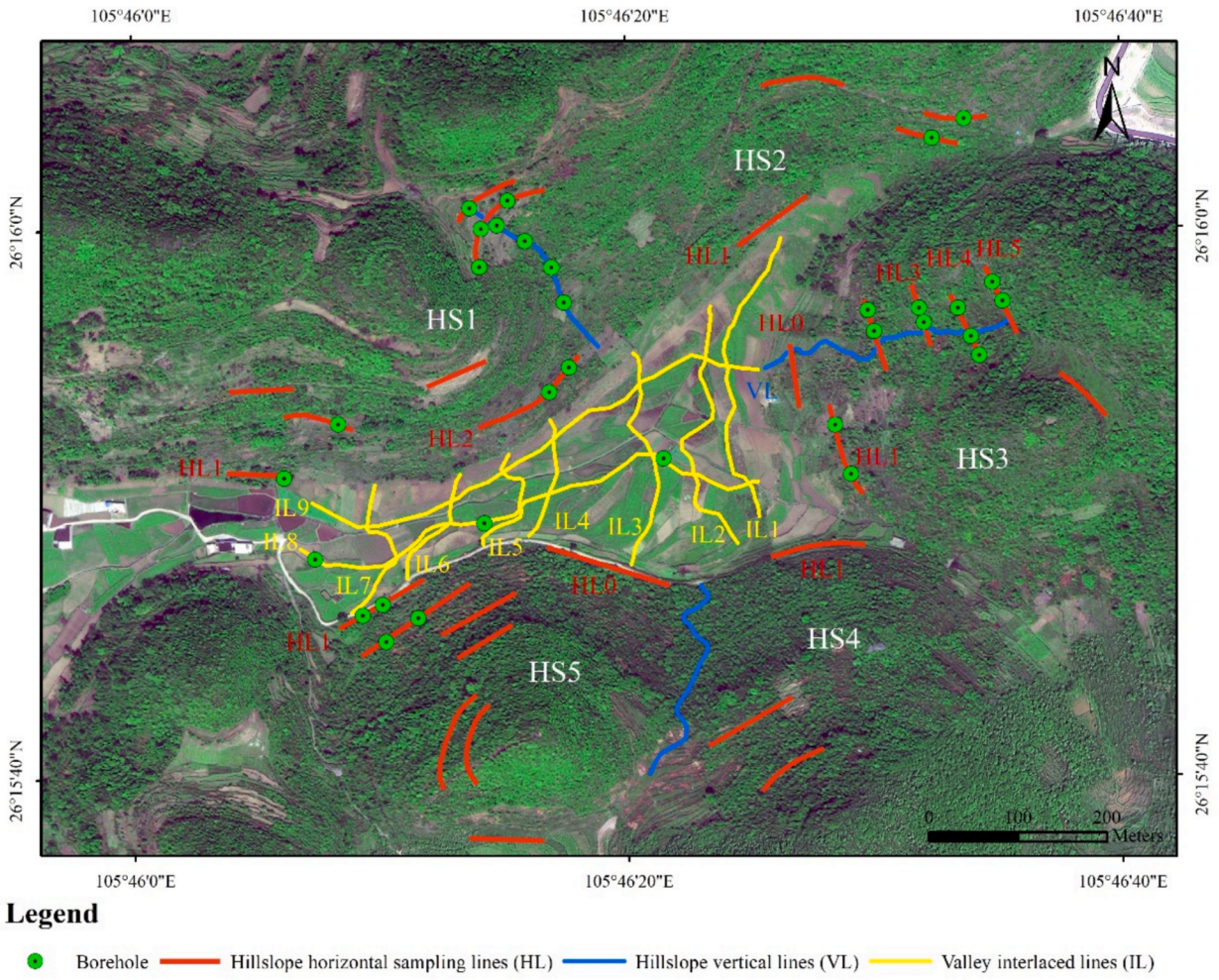

Fig. 2. Distribution map of horizontal and vertical sampling lines in the hillslopes (HS1-HS5), interlaced sampling lines in the valley, and location of boreholes within the catchment.

thin limestone, and HS3-HL5 with thick limestone) were selected as representative cases to describe the interpretation method (Figs. 3-4). We then divided all extracted 1D ρ profiles into two types. The first type has clear inflexion points, reflecting the soil-epikarst-compact bedrock interfaces (Fig. 3b and 3c). The second type has unobvious or multiple inflexion points because of complex environmental conditions such as high moisture content and rock fragmentation degree, soil filling beneath the rock layer, and small resistivity comparison between soil and thin limestone. Thus, these uncertain inflexion points need further revision (Fig. 3d-3f, Fig. 4b). The specific steps are as follows:

i. The 1D profiles of each sampling point along a sampling line were extracted in the vertical direction (Fig. 3a). The first clear inflexion point appearing in the upper part of the 1D profile corresponds to the depth and resistivity value of the inferred soil-epikarst interface. The second clear inflexion point appearing in the lower part of the 1D profile corresponds to the depth and resistivity value of the inferred epikarst-compact bedrock interface (Fig. 3b-c)
ii. The clear inflexion points for the 1D profiles of other sampling points were obtained similarly. Subsequently, the range of resistivity for the soil-epikarst interface (16–65 Ω m in Fig. 3a) and epikarst-compact bedrock interface (1310–2274 Ω m in Fig. 3a) of most of the sampling points can be preliminarily obtained
iii. Regarding the soil-epikarst interface, the inflexion points of some sampling points are unclear and uncertain, which need to be compared and corrected. For example, the depth between the first two inflexion points should be the soil layer if rocks cover the soil (Fig. 3d). When the epikast is highly fragmented or has a high moisture content below the soil, several uncertain inflexion points may appear (Fig. 3e). It is also necessary to replace the uncertain inflexion point (ρ = 117 Ωm, depth = 1.03 m in Fig. 3f) with the revised inflexion point (ρ = 32 Ωm, depth = 0.25 m in Fig. 3f) according to the limited interface resistivity range by the priori clear inflexion points (16–65 Ω m in Fig. 3a) obtained in step **ii.** Because of the low resistivity of thin limestone bedrock, there is no obvious inflexion point between soil and epikarst (Fig. 4b). In this case, using interface resistivity range obtained by other priori clear inflexion points of its adjacent sampling points in the same line to correct it (Fig. 4c)
iv. There is also some uncertainty when estimating the location of the epikarst-compact bedrock interface. Some unclear inflexion points can be corrected by comparing the epikarst-compact bedrock interface resistivity values with adjacent sampling points (Fig. 3d). When there is a relatively continuous, thick, and high resistivity rock above the uncertain inflexion point (for instance, thin limestone is overlaid with thick limestone) (Fig. 4e-f), the lower uncertain point (ρ = 390 Ω m) must be replaced. As such, this should be replaced by a revised point above the high resistivity rock (ρ = 5200 Ω m in Fig. 4f) because the above layer is compact and not dissolved

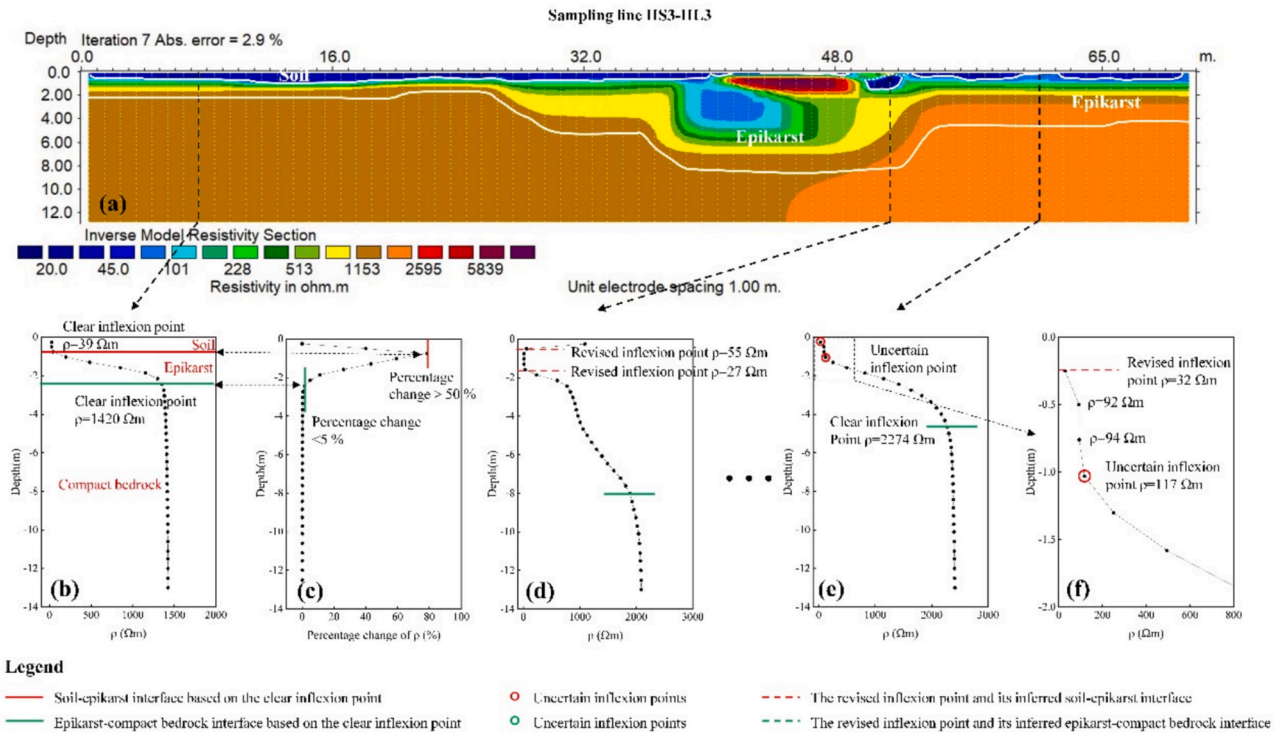

Fig. 3. Schematic diagram of the 2D resistivity (ρ) image based on sampling line HS3-HL3 inversion **(a)** and of soil-epikarst-compact bedrock interface determined by the vertical 1D ρ profiles of each sampling point **(b-f)**. The 2D ρ image (a) 's white lines represent the interpreted soil-epikarst-compact bedrock interface.

v. By horizontally connecting all sampling points' clear and revised inflexion points, a continuous soil-epikarst and epikarst-compact bedrock interface can be obtained (Fig. 3a and 4a). In rare cases, soil in karst areas fills dissolution fractures and wedges beneath the rock layer without being exposed at the surface (Fig. 3d). Thus, the rock thickness above the soil must be removed when estimating ST (Fig. 3d). Otherwise, the actual ST and soil stock will be overestimated. Then, repeat the above steps for the other sampling lines (Fig. 4g)

vi. We used 50, 100, and 300 Ωm ρ isopleth thresholds to delineate the soil-epikurst interface, respectively (Chen et al., 2018; Cheng et al., 2019a; Luo et al., 2024). We also used 400, 1000, and 3000 Ωm ρ isopleth thresholds to delineate the epikarst-compact bedrock interface, respectively (Chen et al., 2018; Cheng et al., 2019a). Notably, these were used to compare the interpretation performance of the methods proposed in this study

2.4. Data validation

Thirty-two boreholes were obtained at locations of key sampling lines in the catchment to validate the interpreted ST and EkT (Fig. 2). The drilling depths ranged from 4 to 22 m, with an average depth of 7.6 m (Fig. 5). The soil-epikarst interface is clear in the extracted drilling cores, and ST can be directly measured. Following the Chinese standard for engineering classification of rock masses (GB50218-94), the compact bedrock depth and EkT was determined based on rock fragmentation, fissure development degree, fissure density, and bedrock integrity degree of drilling cores (Wang et al., 2024). The validation accuracy of ST and EkT was evaluated using coefficient of determination (R^2) and root mean square error (RMSE).

2.5. Statistical analysis and variable selection

Statistical analysis of ST and EkT was conducted using SPSS19.0 software. The ST and EkT spatial distribution maps, based on 5268 sampling points in the catchment, was generated using the ordinary kriging method performed by ArcGIS 10.2 geostatistical tool (Fig. 6a, Fig. 6b).. A semi-variogram function identified the best fit model for spatial interpolation and the spatial structure of the interpolated ST and EkT. A total of 25 quantitative, semi-quantitative, and qualitative environmental variables were collected within the catchment (Table 2). Using a unified resolution is a prerequisite for subsequent modelling, as mismatched resolutions can significantly increase noise and lead to spatial inconsistencies in model input data (Abbaszadeh Shahri et al., 2019; Mishra et al., 2023). Among these, 18 quantitative topographic variables including primary and secondary attributes were produced from terrain data with a resolution of 12.5-meter raster. Primary attributes such as elevation, slope, and aspect were calculated using ArcGIS 10.2, while secondary attributes such as topographic wetness index, flow length up, and stream power index were calculated by spatial analysis tools (Zhang et al., 2022). The two semi-quantitative variables ST and EkT, with an initial resolution of 1 m, were resampled to 12.5 m. A total of 614 grids were generated for subsequent modelling (Fig. 6c). Five qualitative environmental variables were parameterized, and subsequently converted into a 12.5-meter raster. The environmental variables were georeferenced to the EkT raster, ensuring spatial matching of all grid cells (Rosin et al., 2025).

Three models including multiple linear regression (MLR), random forest (RF), and extreme gradient boosting (XGBoost) , were used to assess feature importance between environmental variables and EkT performed by Python 3.10.0. These two machine learning algorithms (RF and XGBoost) used MLR as a baseline model, with hyperparameters tuned via random search. Sensitivity analysis incorporated multi-model consensus validation, whereby key common variables were identified by comparing feature importance rankings across the three models. Feature weights were derived from coefficients in MLR and from built-in feature importance metrics in RF and XGBoost. Consistency in feature importance rankings across models demonstrated the robustness of the analysis to model selection. Model performance was evaluated using R^2 and RMSE. The three models were calculated in the hillslope, valley, and

Table 1
ERT survey and soil-epikarst thickness statistics for the hillslopes, valley, and catchment.

Landform	ERT lines number	Sampling points number	Sampling length (km)	Soil thickness					Epikarst thickness			
				Maximum (m)	Average (m)	Standard Deviation	Coefficient of Variation		Maximum (m)	Average (m)	Standard Deviation	Coefficient of Variation
HS1	8	1080	1.08	2.15	0.47	0.40	0.86		9.14	4.21	2.31	0.58
HS2	4	660	0.66	2.15	0.42	0.43	1.03		8.17	4.58	2.26	0.49
HS3	8	973	0.97	2.74	0.48	0.45	0.93		9.45	3.99	2.62	0.66
HS4	3	336	0.33	2.44	0.50	0.49	0.98		9.85	4.53	3.08	0.68
HS5	9	864	0.86	3.35	0.52	0.47	0.91		8.17	3.38	2.53	0.75
All hillslopes	32	3913	3.9	3.35	0.49	0.45	0.92		9.85	3.93	2.57	0.65
Valley	9	1355	2.7	9.32	3.23	1.62	0.50		23.94	3.77	2.94	0.78
Catchment	41	5268	6.6	9.32	1.23	1.55	1.26		23.94	3.91	2.95	0.74

catchment, respectively. Feature importance values reflect the relative influence of each variable on EkT, with higher values indicating stronger influence.

3. Results

3.1. Interpretation and verification of soil-epikarst-compact bedrock interfaces

Although the vertical distance between the three sampling lines (HS3-HL3, HS3-HL4, HS3-HL5) is less than 110 m (Fig. 2), their bedrock resistivity shows a significant difference with 500–26000 Ω m (Fig. 3a, 4a, and 4 g). Due to the complex rock and soil structure for each sampling line along the hillslope, the soil-epikarst-compact bedrock interface for each sampling line/point were independently interpreted in this study (Fig. 4). The interpreted resistivity range of the soil-epikarst interface of all sampling lines is 6–92 Ωm, and the resistivity range of the epikarst-compact bedrock interface is 350–7800 Ω m. For the given sampling points along the survey line HS3-HL4 at 14 m and 51 m, the interpreted depths of the soil-epikarst interface and epikarst-compact bedrock interface using the revised inflexion point of the 1D resistivity profile were 0.25 and 1.03 m, respectively (Fig. 4 b and e). The borehole core measurement depths were 0.32 and 1.38 m for these interfaces (Fig. 4a). This validates reliability with this study's revised inflexion point. Overall, a good fitting performance was demonstrated for both ST (R^2 = 0.91, RMSE = 0.18 m) and EkT (R^2 = 0.76, RMSE = 0.96 m) utilizing clear and revised inflexion points in the proposed method (Fig. 5). Compared with the inferred results using inflexion points before revision and other specific resistivity isopleth thresholds, the results using revised inflexion points significantly improves the interpretation accuracy. Notably, the R^2 of ST increased by 0.53, and the RMSE decreased by 1.93 m (Fig. 5a); The R^2 of EkT increased by 0.62, and the RMSE decreased by 5.72 m (Fig. 5b). Thus, our results demonstrated that when estimating soil-epikarst-compact bedrock interfaces in complex lithological sites with significant differences in resistivity, no specific resistivity isopleth threshold can be used between inter-sampling lines or even inter-points. There is also uncertainty and estimating errors without revising the inflexion points in sites with complex rock and soil structures, fragmented epikarst zone, high moisture content, thin limestone with small resistivity, and different lithological coverage (Fig. 3, Fig. 4, Fig. 5).

3.2. Geostatistical analysis of ST and EkT

Compared to the other models, the exponential model has the highest R^2 and the lowest Residual sum of squares. Therefore, the exponential model was used to obtain the map of ST and EkT spatial distribution in the catchment (Fig. 6a, Fig. 6b, Table 3). The average ST is 0.42–0.52 m, and the average EkT is 3.38–4.58 m between hillslopes (HS1-HS5) (Fig. 7, Table 1). The average ST (3.23 m) in the valley is significantly greater than in hillslopes (0.49 m) because of as expected within a typical soil toposequence. Although there are some scattered, fragmented areas with EkT over 20 m in the valley, both the average and median EkT (3.77 and 2.98 m) of the valley is slightly smaller than that of hillslopes (3.93 m and 3.63 m) (Fig. 6b, Fig. 7b, Table 1). The ST showed a relatively strong variation degree in hillslopes (coefficient of variation with 0.92), while the EkT had a moderate degree of variation (0.65). However, the opposite situation occurs in the valley, where the variation degree of EkT (0.78) is greater than that of ST (0.5) (Table 1). The statistical relationship between ST and EkT on hillslopes, valleys, and catchments is shown in Fig. 8. Negative correlations were identified for hillslopes, valleys, and catchments when using independent sampling points data (Fig. 8). Although the negative correlation in hillslopes was significant (with p = 0.01), their correlation coefficients are all less than 0.1. Thus, it suggests there may not be a direct relationship between ST and EkT at a meter and small scale.

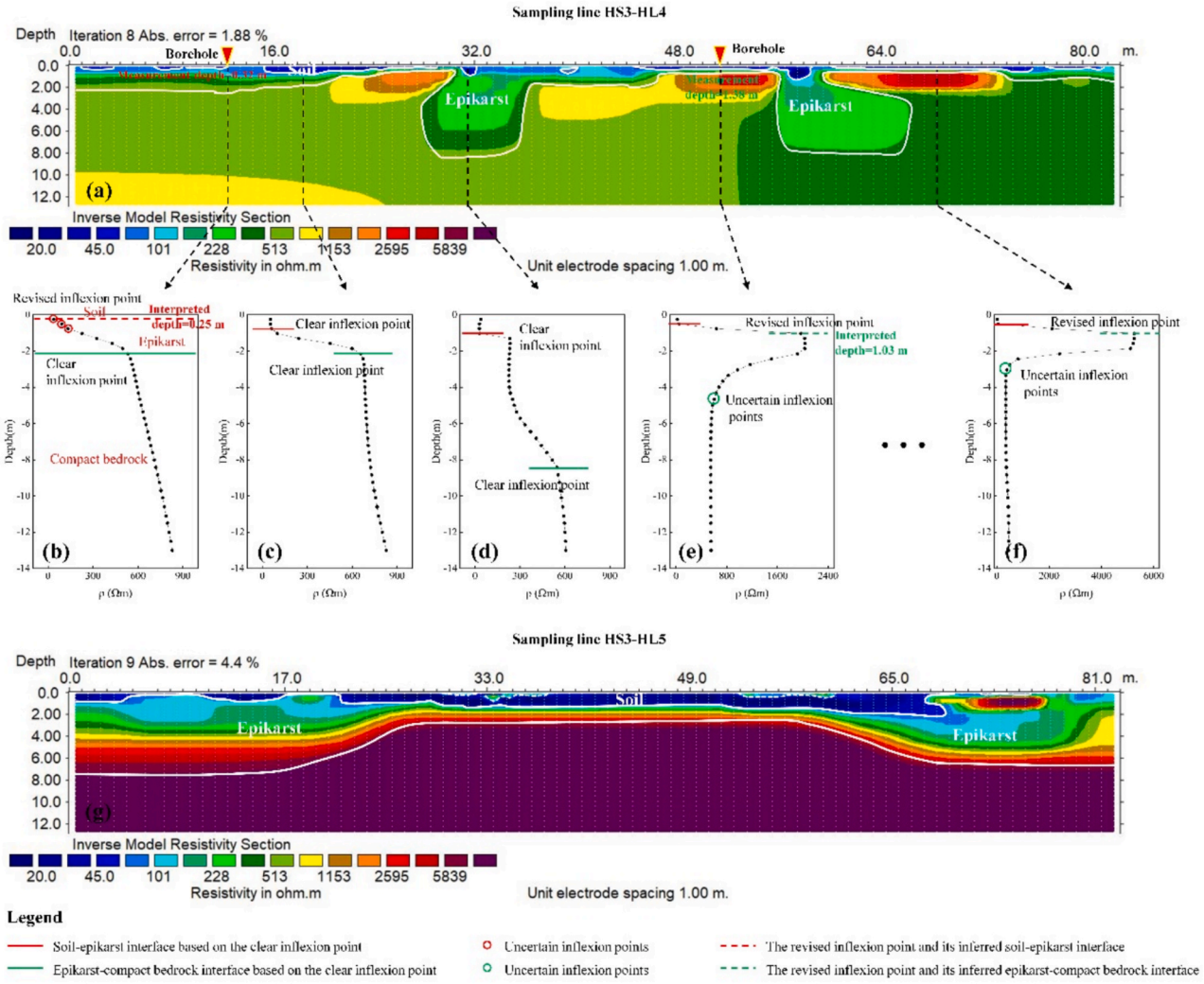

Fig. 4. Schematic diagram of the 2D resistivity (ρ) image based on sampling line HS3-HL4 inversion **(a)** and of soil-epikarst-compact bedrock interface determined by the vertical 1D ρ profiles of each sampling point **(b-f)**. The same method was used to interpret the soil-epikarst-compact bedrock interface for another sampling line, HS3-HL5 **(g)**.

3.3. Heterogeneity of ST and EkT and its zonality variations

The ST and EkT under different slope positions showed synchronous vertical zonality along the hillslope. Large ST and EkT are observed at the downslope and saddle. At the same time, smaller thicknesses on the upslope and middle slope were noted (Fig. 9a). The continuous sampling results from HS3-VL reflect the discontinuous distribution of both ST and EkT, exhibiting many wedge shapes and strong heterogeneity even at meter scale (Fig. 9b). However, the average ST and EkT show the same vertical variations at different slope positions along the HS3-VL (Fig. 9b). Not all locations have thick soil/epikarst at the downslope when compared in a horizontal circumferential direction (Fig. 6). Spatial distribution of ST/EkT exhibited large difference between concave and convex positions at the downslope along the clockwise loop from HS1 to HS5 (Fig. 6, Fig. 9c). The sampling lines located near the ridge and convex positions have relatively small ST and EkT (HS3-HL0 and HS5-HL0 in Fig. 6 and Fig. 9c). In contrast, lines located below the saddle and near to the concave positions have large EkT (HS1-HL2, HS2-HL1, HS3-HL1, HS4-HL1 and HS5-HL1 in Fig. 6b and Fig. 9c). Among them, HS2-HL1 and HS5-HL1 have large ST, but HS1-HL2, HS3-HL1 and HS4-HL1 have small ST (Fig. 6a, Fig. 9c). Bedrock outcrops are not observed in the valley, and soils exhibit continuous distribution (Fig. 6a). In contrast, the epikarst shows several scattered, fragmented areas, which may be the vertical conduits zone for preferential flow between surface and underground horizontal conduits zone (Fig. 6b). The ST and EkT display synchronous horizontal zonality that increases first and then decreases along the outlet direction in the valley (Fig. 9d). The V-IL3 has largest average ST/EkT in the middle of valley, corresponding to the area below the saddle and as an extension of HS1-VL and HS5-VL (Fig. 6).

3.4. Environmental controlling factors

Fig. 10 shows that the performance of the three models follows the order: MLR < RF < XGBoost. XGBoost achieved relatively higher accuracy ($R^2 > 0.6$) in hillslope, valley, and catchment, and was therefore selected as the optimal model. The 10 most important variables were extracted in the hillslope (in order of Slope position (SP), Aspect (A), Slope (S), Coefficient variation of elevation (CVE), Flow length down (FLD), Flow accumulation (FA), Flow length up (FLU), Elevation (ELE), Plan curvature (PLC), and Curvature (CUV)) (Fig. 10c), in the valley (in order of FLU, CUV, A, Stream power index (SPI), Sediment transport capacity index (STI), ELE, S, PLC, Flow direction (FD), and Flow length down (FLD)) (Fig. 10f), and in the catchment (in order of A, PRC, SPI, ELE, PLC, CVE, FLD, S, Topographic wetness index (TWI), and CUV) for further analysis (Fig. 10i). Overall, curvature related variables (CUV,

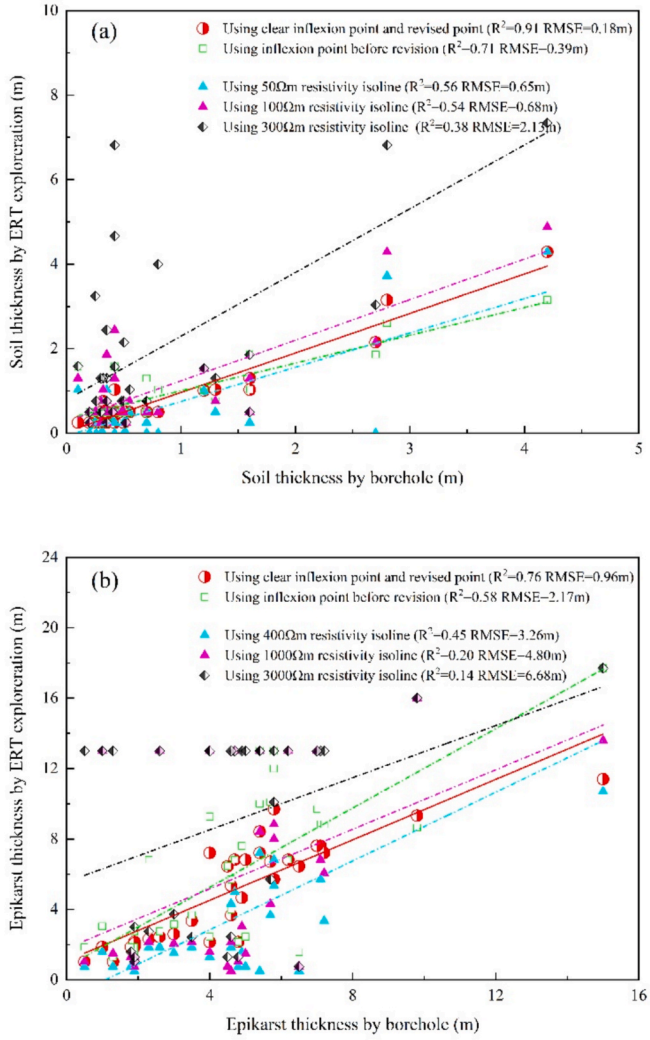

Fig. 5. Comparison of verification accuracy of soil thickness **(a)** and epikarst thickness **(b)** using inflexion points of 1D vertical resistivity profile and specific resistivity isoline thresholds.

PRC, PLC), flow length related variables (FLU/FLD), A, and ELE were screened out as important topographic features affecting EkT in the hillslope, valley, and catchment (Fig. 10c, Fig. 10f and Fig. 10i). CVE and S were screened out in the hillslope and catchment, while SPI was screened out in the valley and catchment.

4. Discussion

4.1. Challenges and uncertainty for ERT interpretation in complex rock and soil structure sites

The borehole verification results indicate that using the same and specific resistivity isopleth threshold to estimate the soil-epikarst-compact bedrock interface for different sampling lines and sites has extensive errors (Fig. 5). With differences in the composition, moisture content, and purity between sites, both the soil-epikarst interface and epikarst-compact bedrock interface may have varying resistivity values (Coulouma et al., 2013; Tao et al., 2021). Therefore, we believe sites with complex lithological types and significant differences in resistivity require independent interpretation of each ERT sampling line/point. Previous studies have shown challenges and uncertainties when interpreted with complex rock and soil structures. This means some inflexion points must be revised to reduce uncertainty during interpretation. The rock barrier effect caused by overlying rocks leads to overestimating ST (Luo et al., 2024). The subsurface's fragmented and high moisture content led to varying inflexion points in the soil-epikarst interface (Coulouma et al., 2013). Thin limestone has small electrical resistivity, which affects uncertainty in interpreting the soil–bedrock interface (Cheng et al., 2019b). The interpretation of the soil-epikarst interface does not supply satisfactory results when the resistivity variation between certain strata is low or the resistivity contrast is insignificant (Kowalczyk et al., 2015). Thus, this provides evidence for revising these uncertain inflexion points in this study. The vertical 1D resistivity profile within the thin limestone site overlying thick limestone is different from that of other sites with a single lithology (Fig. 4). Nonuniform weathering conditions between the upper thick and lower thin limestone leads to preferential flow, forming local dissolved areas with deep wedge-shaped (Fig. 4a). Interpreting the inflexion point and interface at the position of the dissolved wedges are same as that of most 1D profiles (Fig. 4d). However, the inflexion point needs to be revised above the thick limestone at the undissolved position (Fig. 4e-f). The RMSE of ST/EkT decreased 0.21/1.57 m using the revised inflexion point compared with that using the inflexion point before revision (Fig. 5). This demonstrates the necessity for altering the uncertain and unclear inflexion points to obtain real soil-epkarst-compact bedrock interface in this study.

The resistivity threshold of the interpreted soil-epikarst interface is 6–92 Ωm of all 41 sampling lines, within the common range of soil with less than 100 Ωm (Cheng et al., 2019a). Although the resistivity threshold of the interpreted epikarst-compact bedrock interface has extensive variations with 350–7800 Ωm, it is still within the resistivity range of thick and thin limestone in the previous study (Tao et al., 2021). The testing time for this study was during the period without precipitation or 3 days following precipitation, indicating that the ERT sampling data of subsurface structure are not affected by rainfall events in this study because of rapid hydrological processes in a very small karst catchment (Zhang et al., 2013). Carrière et al. (2013) demonstrated that the ERT method cannot reflect the distribution of fissures. Our result failed to detect those soil distributions inside fissures and fractures, which may slightly underestimate the soil volume and stock. The reliability of physical parameter variation models displayed in ERT apparent resistivity images in areas with complex soil conditions depends on the horizontal and vertical variations in dielectric properties of specific strata and the thickness of these strata (Kowalczyk et al., 2017). Low resistivity variations in specific strata, large electrode spacing, or insufficient validation data from the medium can reduce the reliability of resistivity imaging (Kowalczyk et al., 2015). A previous study has used a 5-meter electrode spacing to estimate the ST/EkT in a catchment scale (Wang et al., 2022). ERT survey conducted in this study with shorter electrode spacing in hillslopes with 1 m and valleys with 2 m, which obtained high resolution with decimeter level ρ data in depth (Figs. 3-4). Based on the borehole observations, the decimeter level resolution of 1D vertical ρ profile is enough to effectively illustrate the soil-epikarst-compact bedrock interface and ST/EkT distributions at the catchment scale.

4.2. Spatial heterogeneity of ST and EkT and its controlling factors in limestone catchment

Wang et al. (2022) found the average EkT of depression is much greater than that of hillslope in the peak cluster-depression catchment. This is likely related to the closure depression leading to abundant runoff in the form of vertical infiltration, promoting the development of karst zones in the depression (Wang et al., 2024). However, the peak cluster-valley catchment shows a difference in that the average ET of the valley is smaller than that of the hillslope (Fig. 7b). On the one hand, after runoff from the hillslope merges into the valley, the preferential flow quickly enters the surface river and underground horizontal conduits by sinkholes and vertical conduits, and discharges into the surface/

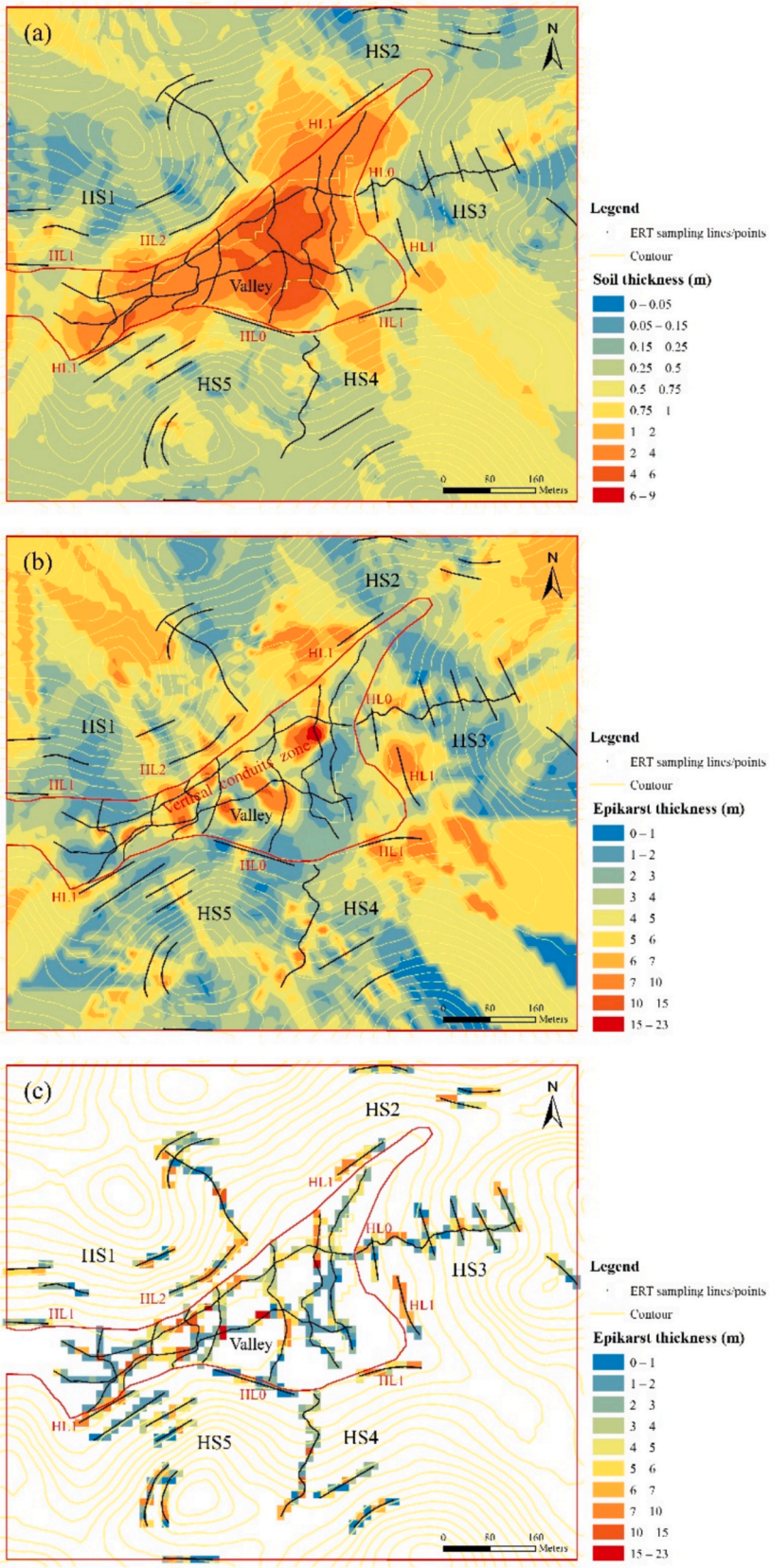

Fig. 6. Spatial distribution map of soil thickness **(a)** and epikarst thickness **(b).** The resampled epikarst thickness grids in the catchment **(c).**

Table 2
Summary and description of 25 quantitative, semi-quantitative, and qualitative environmental variables based on the catchment's topographic, geophysical, and soil data.

Category	Environmental variables	Abbreviation	Units	Description
Quantitative	Aspect	A	°	Primary and secondary variables produced from terrain data with a resolution of 12.5-meter raster, calculated by ArcGIS/performing surface and hydrology in the spatial analysis tool.
	Curvature	CUV		
	Coefficient variation of elevation	CVE	%	
	Elevation	ELE	m	
	Flow accumulation	FA	m^3	
	Flow direction	FD		
	Flow length down	FLD	m	
	Flow length up	FLU	m	
	Land relief	LR	m	
	Plan curvature	PLC		
	Profile curvature	PRC		
	Slope	S	°	
	Specific catchment area	SCA	m^2/m	
	Surface cutting depth	SCD	m	
	Stream power index	SPI		
	Sediment transport capacity index	STI		
	Topographic roughness index	TRI		
	Topographic wetness index	TWI		
Semi-quantitative	Soil thickness	ST	m	Data from ERT, with a resolution of 1 m, and was resampled to 12.5 *m*
	Epikarst thickness	EkT	m	Data from ERT, with a resolution of 1 m, and was resampled to 12.5 *m*
Qualitative	Landform type	LAT		Classified as hillslope and valley
	Land cover type	LC		Classified as paddy field, cultivated land, forest, shrub and grass
	Lithology type	LIT		Classified as dolostone, thick limestone, thin limestone, and marlstone
	Slope position	SP		Classified as upslope, saddle, middle slope, and downslope
	Soil type	STY		Classified as paddy soil and limestone soil

Table 3
Types and parameters of the semi-variogram model for the catchment's soil and epikarst thickness.

Category	Sample number	Model	Nugget Co	Sill variance Co + C	Co/C + Co (%)	Range (m)	R^2	Residual sum of squares
Soil thickness	5268	Spherical	0.07	3.15	2.23	212.0	0.966	0.049
		Gaussian	0.32	2.88	11.05	163.4	0.919	0.109
		Circular	0.08	3.13	2.62	186.1	0.964	0.051
		Stable	0.21	3.04	7.01	191.3	0.941	0.080
		Exponential	0.03	3.58	0.86	343.4	0.972	0.039
Epikarst thickness	5268	Spherical	1.24	10.46	11.83	43.7	0.918	0.326
		Gaussian	2.54	9.04	28.05	34.6	0.895	0.586
		Circular	1.41	10.28	13.70	39.1	0.910	0.359
		Stable	0.09	12.44	0.71	60.4	0.956	0.094
		Exponential	0.07	12.15	0.58	54.0	0.978	0.088

underground outlets. The horizontal flow is dominant, and the proportion of vertical infiltration is minute, limiting the development of the epikarst zone in the valley (Cheng et al., 2019a). On the other hand, the weathering rate is highest when the soil is of medium thickness, while the weathering rate is slow when the soil is very thick or thin (Dong et al., 2019a; Dong et al., 2019b). Notably, the valley has a very large average ST with 3.23 m (Table 1), and the long vertical distance limits the transmission of water, CO_2, and biological acid sources to bedrock, resulting in a slow weathering rate and a thin epikarst zone formation.

The GLM exhibited poor model performance ($R^2 < 0.1$) and failed to effectively identify influential variables (Fig. 10), due to the nonlinear relationship between topographic-vegetation variables and EkT (Zhang et al., 2022). XGBoost achieved higher predictive accuracy than RF across hillslope, valley, and catchment, a finding consistent with Li et al. (2020) who compared four models including XGBoost, RF, support vector regression, and GLM in modelling ST and identified XGBoost as the optimal model. Curvature-related factors (CUV, PRC, PLC), flow length (FLU/FLD), Aspect, and ELE are most important variables that affect EKT in the hillslope, valley, and catchment. Flow is easier to accumulate in concave locations with negative PLC and positive PRC, improving the dissolution conditions and causing well-developed epikarst and larger EkT. Higher flow length values indicate water travels a longer distance across hillslopes, resulting in extended contact time and enhanced dissolution in the epikarst. Curvature and flow length have been demonstrated as key factors influencing ST/EkT in karst areas (Kuriakose et al., 2009; Liu et al., 2013; Wang et al., 2022). In the downslope with different curvatures, small ST/EkT was observed due to poor dissolution conditions and soil erosion in the areas at convex positions (Fig. 6a, Fig. 9c). The areas below the saddle and near the concave positions have good hydrological conditions and dissolution environment, resulting in large EkT. However, soil erosion and sedimentation may occur in these concave positions because of different vertical topography features. Thus, the ST of the areas may be thick or thin (Fig. 6a, Fig. 9c). Srivastava et al. (2024) noted that south-facing slope and north-facing slope exhibit distinct solar radiation levels and vegetation distribution. HS2 is both a south-facing slope and a windward slope in the Chenqi catchment. Compared to other hillslopes, it likely experiences higher solar radiation and larger rainfall amount, thereby promoting the development of the epikarst zone. Consequently, the greatest average EkT was observed at HS2 among the hillslopes (Fig. 7b). ELE may influence EkT indirectly through other topographic variables in this study area. However, both upstream and downstream in

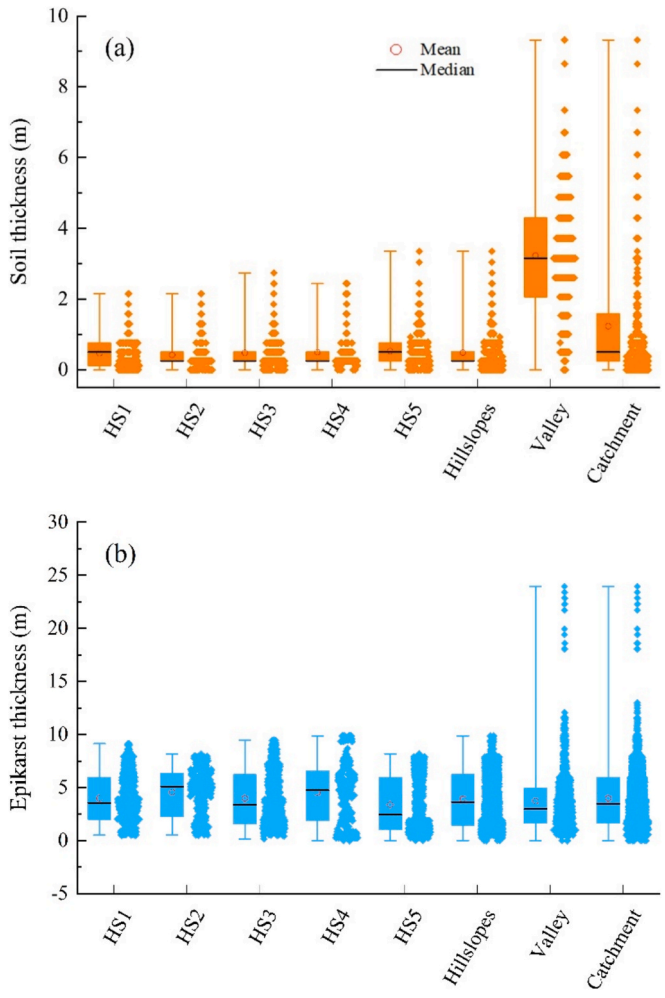

Fig. 7. Soil thickness **(a)** and epikarst thickness **(b)** of hillslopes, valleys, and catchment.

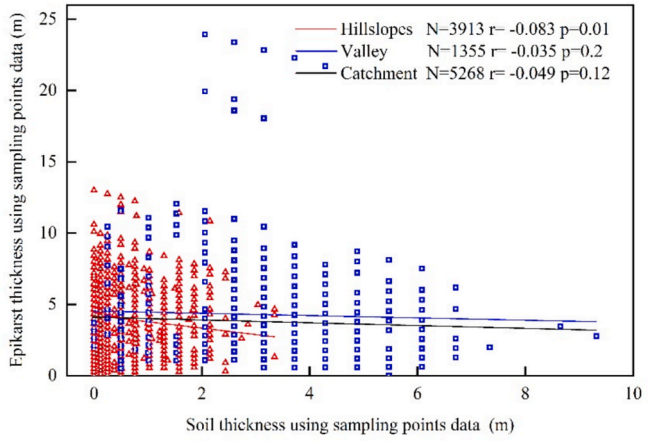

Fig. 8. The relationship between soil thickness and epikarst thickness using sampling point. *N* is the sample number, *r* is the correlation coefficient, and *p* is the significance value.

karst regions may have well developed and poorly developed epikarst (Pardo-Igúzquiza et al., 2018), suggesting that ELE may not be suitable for predicting EkT at large scales. Previous studies modeling ST across different scales achieved consistent results. ELE was identified as a factor influencing ST in the 9.5 km^2 small catchment scale, while ELE was no longer selected as an influencing factor in the 76 km^2 catchment scale (Kuriakose et al., 2009; Zhang et al., 2022).

Different key variables were screened out in the hillslope, valley, and catchment. SP was ranked as the first order variable in the hillslope, which reflects the vertical zonality variation of EkT under different slope positions (Huang et al., 2021; Zhang et al., 2013). S and CVE were identified as important variables in both the hillslope and catchment, whereas they were not selected in the valley. This discrepancy may be explained by the fact that variations in S and CVE are still captured within the 12.5 m resolution within the hillslope and catchment. In contrast, the relatively flat valley exhibits low local variability of S and CVE, making subtle terrain differences difficult to detect. The reduced local variability of variables leads to their contributions being averaged, and consequently, they are likely to be overlooked (Han et al., 2025). ST was identified as a predictor of EkT in valleys, consistent with findings by Wang et al. (2022) and Wang et al. (2024). However, ST was not considered an important variable in slopes or catchment (Fig. 10), as curvature-related variables exerted larger influence on ST/EkT distribution in the downslope, thereby diminishing the importance of ST and SPI in the hillslope and catchment. The complexity of the ST formation process results in strong heterogeneity even within a small scale (Luo et al., 2024). Although using point data showed a significant negative correlation between ST and EkT (Fig. 8), we consider that there may not be a direct relationship between them on a small scale. Our results suggest that EkT modelling should be based on landform units rather than the entire catchment. Although evidence suggests that variables such as land cover type, and lithology are related to soil thickness and epikarst development (Brosens et al., 2021; Li et al., 2020; Zhong et al., 2022), this study did not obtain such results. The possible reason is that the Chenqi catchment has a very small area and is affected by human activities. Perhaps the importance of vegetation, land cover type, and lithology will be more highlighted when compared to large-scale natural catchments or inter-sites.

Key controlling variables influencing EkT were identified using a resolution of 12.5 m raster in a small catchment. The selected variables can serve as a reference for spatial EkT prediction in other karst regions, since publicly accessible global DEM products typically range from 12.5 to 30 m (Ortíz-Rodríguez et al., 2022). Methods utilizing machine learning approaches and multi-source data fusion to enhance image resolution and delineate 3D subsurface structures have been previously proposed (Abbaszadeh Shahri et al., 2020; Abbaszadeh Shahri et al., 2024; Ren et al., 2025; Doyoro et al., 2025). Future work will focus on the utilization of these methods to delineate a high-resolution EkT distribution map, followed by a comparative analysis against results obtained at the current resolution.

5. Conclusion

This study investigated the soil-epikarst structure and its spatial distribution in a limestone karst catchment based on ERT. The soil-epikarst-compact bedrock interface and associated ST and EkT at each sampling point were independently interpreted by the clear and revised inflexion point of the 1D vertical resistivity profile. Compared with the estimation results using specific resistivity isopleth thresholds, the estimation results using revised inflexion point significantly reduces the uncertainty of interpretation (the RMSE of ST and EkT decreases by 1.93 and 5.72 m, respectively). This shows that the revised inflexion point of the 1D vertical resistivity profile has advantages in sites of complex rock and soil structures and lithological types with vast differences in resistivity. As a noninvasive and continuous spatial coverage technique, the approach and the interpretation processes used in this study has great promise in visualizing the spatial distribution of soils and epikarst (ST, EkT, soil-epkarst-compact bedrock interface).The average ST of hillslopes and valleys is 0.49 and 3.23 m, respectively, but the average EkT of hillslopes with 3.93 m is slightly larger than that of valleys with 3.77 m. ST and EkT show synchronous zonality variation in different

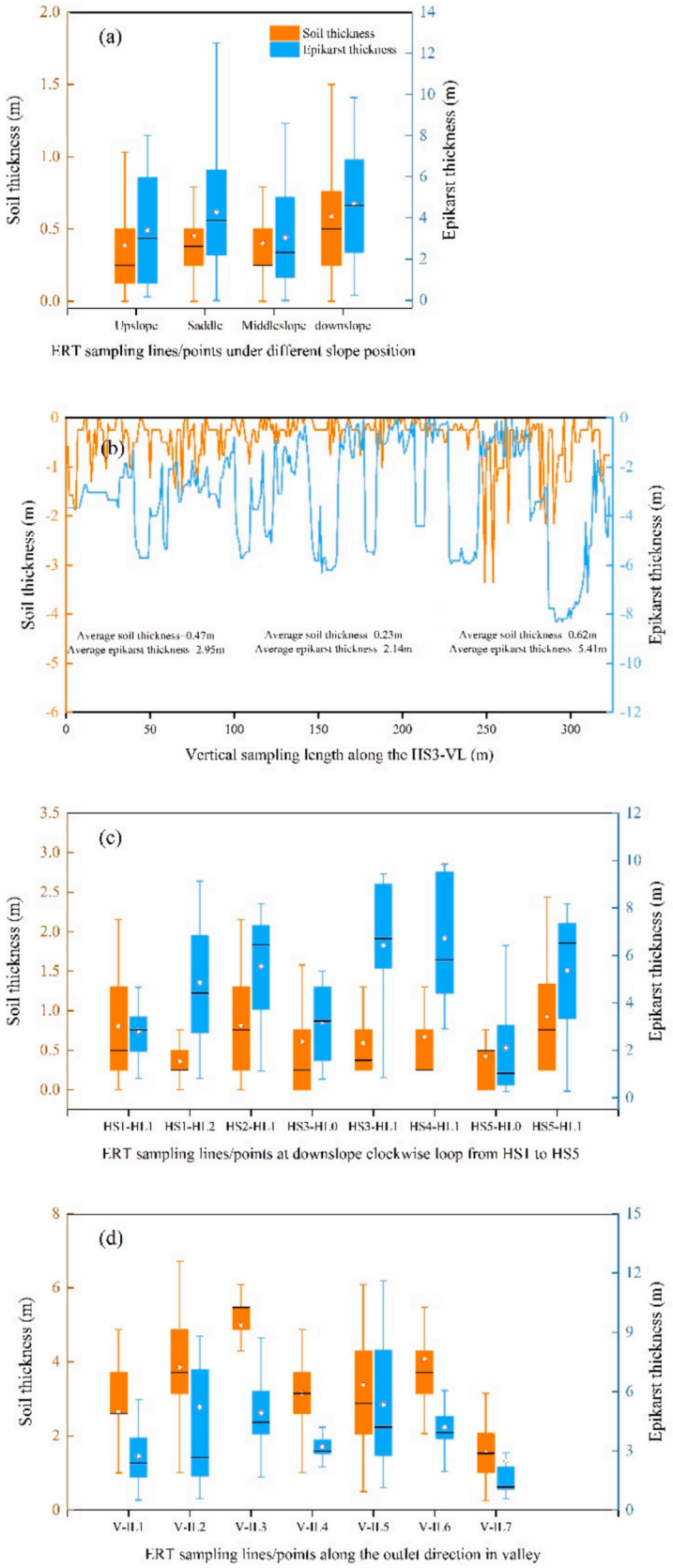

Fig. 9. Heterogeneity of soil thickness and epikarst thickness under different slope positions **(a)**, from the saddle to downslope along the HS3-VL **(b)**, and at downslope with a clockwise loop from HS1 to HS5 **(c)** and along the outlet direction in the valley **(d).**

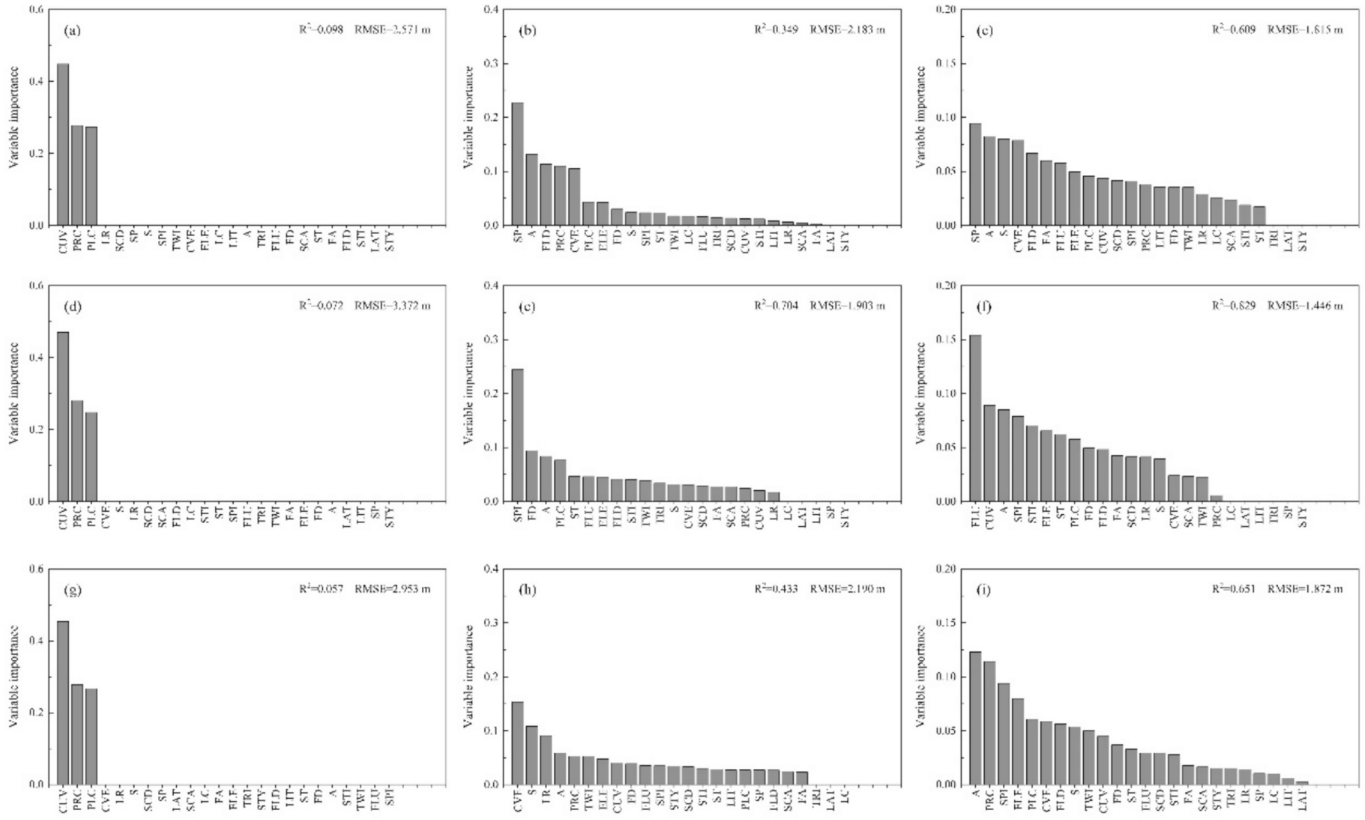

Fig. 10. Importance order of environmental variables affecting epikarst thickness selected by Generalized Linear Regression, Random Forest, and Extreme Gradient Boosting in the hillslopes **(a-c)**, valley **(d-f)**, and catchment **(g-i)**, respectively.

slope positions and valley. The important topographic controlling factors, including PLC, PRC, FLU, FLD, A, and ELE affecting EkT, were screened out by machine learning. The findings of this study can provide crucial underground structure information and parameter support for modelers.

CRediT authorship contribution statement

Weiwei Jiang: Writing – review & editing, Writing – original draft, Software, Methodology, Investigation, Formal analysis, Data curation. **Tao Peng:** Writing – review & editing, Supervision, Funding acquisition, Conceptualization. **Xingbao Zhang:** Methodology, Investigation, Conceptualization. **Shijie Wang:** Resources, Conceptualization. **Zargham Mohammadi:** Writing – review & editing. **Zhanyu Tang:** Writing – review & editing.

Declaration of competing interest

The authors declare that they have no known competing financial interests or personal relationships that could have appeared to influence the work reported in this paper.

Acknowledgments

This study was jointly supported by the National Natural Science Foundation of China (42261144672, 42077317, 42230509, 42407118), Program for Department of Science and Technology in Guizhou Province (ZK[2022]048, [2022]114, GCC[2023]059) and National Key Research and Development Program of China (2023YFF0806002). We are especially grateful to the editor and four anonymous reviewers for their valuable suggestions, which have improved the quality of the manuscript. The authors thank AiMi Academic Services (www.aimieditor.com) for English language editing and review services.

Data availability

Data will be made available on request.

References

Abbaszadeh Shahri, A., Larsson, S., Renkel, C., 2020. Artificial intelligence models to generate visualized bedrock level: a case study in Sweden. Modeling Earth Systems and Environment 6 (2), 1509–1528.

Abbaszadeh Shahri, A., Shan, C., Stefan, L., 2024. A hybrid ensemble-based automated deep learning approach to generate 3D geo-models and uncertainty analysis. Eng. Comput.-Germany 40, 1501–1516.

Abbaszadeh Shahri, A., Spross, J., Johansson, F., Larsson, S., 2019. Landslide susceptibility hazard map in southwest Sweden using artificial neural network. Catena 183, 104225.

Alamry, A.S., Mark, V.D.M., Noomen, M., Addink, E.A., Van Benthem, R., De Jong, S.M., 2017. Spatial and temporal monitoring of soil moisture using surface electrical resistivity tomography in Mediterranean soils. Catena 157, 388–396.

Al-Fares, W., Bakalowicz, M., Guérin, R., Dukhan, M., 2002. Analysis of the karst aquifer structure of the Lamalou area (Hérault, France) with ground penetrating radar. J. Appl. Geophys. 51 (2), 97–106.

Alfuqara, D., Anderson, N., 2023. Geophysical site assessment of soil and the rock structure in karst terrain using 2D and 3D mapping of noninvasive electrical resistivity tomography—southwestern of MO, USA. Arab. J. Geosci. 16, 103.

Alao, J.O., Lawal, K.M., Dewu, B.B.M., Raimi, J., 2024. Detection of shallow underground targets using electrical resistivity tomography and the implications in civil/environmental engineering. Discover Geoscience 2, 52.

Binley, A., Hubbard, S.S., Huisman, J.A., Revil, A., Robinson, D.A., Singha, K., Slater, L. D., 2015. The emergence of hydrogeophysics for improved understanding of subsurface processes over multiple scales. Water Resour. Res. 51, 3837–3866.

Brosens, L., Robinet, J., Pelckmans, I., Ameijeiras-Mario, Y., Govers, G., Opfergelt, S., Minella, J., Vanderborght, J., 2021. Have land use and land cover change affected soil thickness and weathering degree in a subtropical region in Southern Brazil? Insights from applied mid-infrared spectroscopy. Catena 207, 105698.

Carrière, S.D., Chalikakis, K., Sénéchal, G., Danquigny, C., Emblanch, C., 2013. Combining Electrical Resistivity Tomography and Ground Penetrating Radar to study geological structuring of karst Unsaturated Zone. J. Appl. Geophys. 94 (4), 31–41.

Celico, F., Naclerio, G., Bucci, A., Nerone, V., Celico, P., Carcione, M., Allocca, V., Celico, P., 2010. Influence of pyroclastic soil on epikarst formation: A test study in southern Italy. Terra Nova 22 (2), 110–115.
Chalikakis, K., Plagnes, V., Guerin, R., Valois, R., Bosch, F.P., 2011. Contribution of geophysical methods to karst-system exploration: an overview. Hydrogeol. J. 19 (6), 1169–1180.
Chen, X., Zhang, Z., Soulsby, C., Cheng, Q., Binley, A., Jiang, R., Tao, M., 2018. Characterizing the heterogeneity of karst critical zone and its hydrological function: an integrated approach. Hydrol. Process. 32 (19), 2932–2946.
Cheng, Q., Chen, X., Tao, M., Binley, A., 2019a. Characterization of karst structures using quasi-3D electrical resistivity tomography. Environ. Earth Sci. 78 (9), 285.
Cheng, Q., Tao, M., Chen, X., Binley, A., 2019b. Evaluation of electrical resistivity tomography (ERT) for mapping the soil–rock interface in karstic environments. Environ. Earth Sci. 78 (15), 439.
Coulouma, G., Lagacherie, P., Samyn, K., Grandjean, G., 2013. Comparisons of dry ERT, diachronic ERT and the spectral analysis of surface waves for estimating bedrock depth in various Mediterranean landscapes. Geoderma 199, 128–134.
Dong, X., Cohen, M.J., Martin, J.B., Mclaughlin, D.L., Brad Murray, A., Ward, N.D., Flint, M.K., Heffernan, J.B., 2019a. Ecohydrologic processes and soil thickness feedbacks control limestone-weathering rates in a karst landscape. Chem. Geol. 527, 118774.
Dong, X., Murray, A.B., Heffernan, J.B., 2019b. Ecohydrologic feedbacks controlling sizes of cypress wetlands in a patterned karst landscape. Earth Surf. Proc. Land. 44 (5), 1178–1191.
Doyoro, Y.G., Gelena, S.K., Lin, C.P., 2025. Improving subsurface structural interpretation in complex geological settings through geophysical imaging and machine learning. Eng. Geol. 344, 107839.
Gao, Q., Wang, S., Peng, T., Peng, H., David, M.O., 2020. Evaluating the structure characteristics of epikarst at a typical peak cluster depression in Guizhou plateau area using ground penetrating radar. Geomorphology 364, 107015.
Han, X., Liu, J., Wu, P., Yu, Z., Qiao, X., Yang, H., 2025. Predicting the thickness of alpine meadow soil on headwater hillslopes of the Qinghai-Tibet Plateau. Geoderma 456, 117271.
Hartmann, A., Goldscheider, N., Wagener, T., Lange, J., Weiler, M., 2014. Karst water resources in a changing world: Review of hydrological modeling approaches. Rev. Geophys. 52 (3), 218–242.
Huang, X., Zhang, Z., Zhou, Y., Wang, X., Zhang, J., Zhou, X., 2021. Spatial Heterogeneity of Soil Thickness and Factors Controlling It in a Karst Basin. Eurasian Soil Sci.+ 54 (4), 478–486.
Jenny, H., 1941. Factors of soil formation: a system of quantitative pedology. Soil Sci. 52 (5), 415.
Kowalczyk, S., Zawrzykraj, P., Malakowski, M., 2017. Application of the electrical resistivity method in assessing soil for the foundation of bridge structures: A case study from the Warsaw environs. Poland. Acta Geodyn. Geomater. 14 (2), 221–234.
Kowalczyk, S., Zwrzykraj, P., Mieszkowski, R., 2015. Application of electrical resistivity tomography in assessing complex soil conditions. Geol. Q. 59 (2), 367–372.
Kuriakose, S.L., Devkota, S., Rossiter, D.G., Jetten, V.G., 2009. Prediction of soil depth using environmental variables in an anthropogenic landscape, a case study in the Western Ghats of Kerala. India. Catena 79 (1), 27–38.
Leopold, M., Gupanis-Broadway, C., Baker, A., Hankin, S., Treble, P., 2021. Time lapse electric resistivity tomography to portray infiltration and hydrologic flow paths from surface to cave. J. Hydrol. 593, 125810.
Li, X., Luo, J., Jin, X., He, Q., Niu, Y., 2020. Improving Soil Thickness Estimations Based on Multiple Environmental Variables with Stacking Ensemble Methods. Remote Sens.-Basel 12, 3609.
Liu, J., Chen, X., Lin, H., Liu, H., Song, H., 2013. A simple geomorphic-based analytical model for predicting the spatial distribution of soil thickness in headwater hillslopes and catchments. Water Resour. Res. 49 (11), 7733–7746.
Luo, Z., Lian, J., Nie, Y., Zhang, W., Wang, F., Huang, L., Chen, H., 2024. Improving soil thickness estimations and its spatial pattern on hillslopes in karst forests along latitudinal gradients. Geoderma 441, 116749.
Mishra, V.K., Nareti, U., Kumar, R., Pant, T., Aleem, A., Singh, A., Biable, S.E., 2023. GDF: A novel image fusion approach for compelling depiction of earthly features. Journal of Sensors 9429505.
Oyeyemi, K., Aizebeokhai, A., Metwaly, M., Omobulejo, O., Sanuade, O., Okon, E., 2022. Assessing the suitable electrical resistivity arrays for characterization of basement aquifers using numerical modeling. Heliyon 8, e9427.
Pardo-Igúzquiza, E., Dowd, P.A., Ruiz-Constán, A., Martos-Rosillo, S., Luque-Espinar, J. A., Rodríguez-Galiano, V., Pedrera, A., 2018. Epikarst mapping by remote sensing. Catena 165, 1–11.
Peng, T., Wang, S.J., 2012. Effects of land use, land cover and rainfall regimes on the surface runoff and soil loss on karst slopes in southwest China. Catena 90 (1), 53–62.
Ren, A., Wu, L., Xu, J., Xing, Y., Qiu, Q., Xie, Z., 2025. A deep learning method for 3D geological modeling using ET4DD with offset-attention mechanism. Computers and Geosciences 200, 105929.
Rosin, N.A., Mello, D.C.D., Bonfatt, B.R., Hartemink, A.E., Ferreira, T.O., Silvero, N.E.Q., Poppie, R.R., Mendes, W.D.S., Veloso, G.V., Francelino, M.R., Alves, M.R., Falcioni, R., Dematte, J.A.M., 2025. Mapping soil thickness using a mechanistic model and machine learning approaches. Catena 249, 108621.
Srivastava, A., Yetemen, O., Rodriguez, J.F., Kumari, N., Saco, P.M., 2024. The imprint of coevolving semi-arid landscapes, soil, and vegetation on soil moisture and vegetation variability. Catena 242 (000), 108125.
Tao, M., Chen, X., Cheng, Q., Binley, A., 2021. Evaluating the joint use of GPR and ERT on mapping shallow subsurface features of karst critical zone in southwest China. Vadose Zone J. 21 (1), 20172.
Wang, F., Zhang, J., Lian, J., Fu, Z., Luo, Z., Nie, Y., Chen, H., 2022. Spatial variability of epikarst thickness and its controlling factors in a dolomite catchment. Geoderma 428, 116213.
Wang, S., Fu, Z., Chen, H., Nie, Y., Xu, Q., 2020. Mechanisms of surface and subsurface runoff generation in subtropical soil-epikarst systems: Implications of rainfall simulation experiments on karst slope. J. Hydrol. 2020, 124370.
Wang, S., Yan, Y., Zhao, Y., Fu, Z., Chen, H., 2024. Co-evolution among soil thickness, epikarst weathering degree, and runoff characteristics on a subtropical karst hillslope. J. Hydrol. 628, 130499.
Wilcox, B.P., Taucer, P.I., Munster, C.L., Owens, M.K., Mohanty, B.P., Sorenson, J.R., Bazan, R., 2008. Subsurface stormflow is important in semiarid karst shrublands. Geophys. Res. Lett. 35 (10), L10403.
Williams, P.W., 2008. The role of the epikarst in karst and cave hydrogeology: a review. Int. J. Speleol. 37 (1), 1–10.
Xu, C., Xu, X., Liu, M., Li, Z., Zhang, Y., Zhu, J., Wang, K., Chen, X., Zhang, Z., Peng, T., 2020. An improved optimization scheme for representing hillslopes and depressions in karst hydrology. Water Resour. Res. 56 (5), e2019W–e26038W.
Xu, Y., Wang, S., Bai, X., Shu, D., Tian, Y., 2018. Runoff response to climate change and human activities in a typical karst watershed. SW China. Plos One 13 (3), e193073.
Yamakawa, Y., Kosugi, K., Masaoka, N., Sumida, J., Tani, M., Mizuyama, T., 2012. Combined geophysical methods for detecting soil thickness distribution on a weathered granitic hillslope. Geomorphology 145–146, 56–69.
Zhang, Y., Xu, X., Li, Z., Yi, R., Xu, C., Luo, W., 2022. Modelling soil thickness using environmental attributes in karst watersheds. Catena 212, 106053.
Zhang, Z., Chen, X., Chen, X., Shi, P., 2013. Quantifying time lag of epikarst-spring hydrograph response to rainfall using correlation and spectral analyses. Hydrogeol. J. 21 (7), 1619–1631.
Zhong, F., Xu, X., Li, Z., Zeng, X., Yi, R., Luo, W., Zhang, Y., Xu, C., 2022. Relationships between lithology, topography, soil, and vegetation, and their implications for karst vegetation restoration. Catena 209, 105831.